International Journal of Research in Engineering and Science (IJRES)
ISSN (Online): 2320-9364, ISSN (Print): 2320-9356
www.ijres.org Volume 14 Issue 3 ǁ March 2026 ǁ PP. 76-89

Efficient Hybrid Method Using Bond Graphs Modeling and Convolutional Neural Networks for Accurate Single and Multi-Fault Diagnosis

T. Mekki
Higher Institute of Technological Studies of Sfax (ISET),Tunisia

Abstract: *This paper introduces an improved and fine-tuned hybrid FDI approach that integrates bond graph modeling with CNN-based AI technique to enhance fault diagnosis in complex hybrid dynamic systems. The data comes, essentially, from five faults and are classified into six categories: healthy, valve1, valve2, pump, heat and any combination of these. Notably, the quantitative evaluation of our enhanced HBG-CNN hybrid model demonstrated outstanding performance, achieving a classification accuracy of 100% and an F1 score of 100%. One of the most significant results of this study is that the proposed hybrid model architecture is capable of accurately isolating both single incipient faults and multiple simultaneous faults, highlighting its effectiveness and robustness for fault diagnosis in complex hybrid systems.*

Keywords: *Hybrid system, hybrid bond graph, diagnostic hybrid bond graph, global numerical residual, adaptive thresholds, convolutional neural network: CNN, multiple simultaneous faults. Deep learning*

Date of Submission: 05-03-2026 Date of Acceptance: 15-03-2026

I. Introduction

Many recent researches on hybrid systems have been devoted to the synthesis of control laws that guarantee not only stability, but also good performance [1]. Control algorithms are typically developed under the assumption that the system operates under normal conditions. Unfortunately, when failures occur, these algorithms become inefficient and even dangerous for the system itself or its environment. In order to reach higher performance and more rigorous security specifications,a faultdetection and isolation (FDI) system needs to be implemented. The first step of an FDI procedure consists in generating a set of residuals. These residuals are special signals that reflect the discrepancy between the two behaviors. For processes and systems with complex non-linearity, eliminating all unknown variables is not trivial, e.g., in the presence of algebraic loops, implicit equations, non-invertible functions, etc. However, most symbolically non-resolvable relationships can be numerically solved, in which case, it becomes possible to maximize the number of structurally independent residuals.

Hybrid Bond Graphs (HBGs) are an efficient graphical methodology used for modeling complex systems. In addition to supporting dynamic modeling, they have also demonstrated strong applicability in fault detection and isolation (FDI) of hybrid complex systems.In this paper, hybrid bond graph modeling wasused to derive global analytical redundancy relationships (GARRs) and to obtain the computational model in the case of non-resolvability of equations [2,3,4]. A set of sub-graph substitutions in the hybrid bond graph model are developed. These substitutions directly lead to a form whose inputs are the known variables (measurements, sources and parameters) and whose outputs and the residuals.

An incremental bond graph is used to set up adaptive thresholds for the GARR residuals that account for parameters uncertainties. This is an issue of practical relevance because, on one hand, evaluation of GARRs should be robust with regard to parameter uncertainties, i.e., false indication of faults should be avoided. On the other hand, true faults must be detected.Convolutional Neural Networks (CNNs) are a type of deep learning model designed to automatically extract and learn features from various data types such as imagesor time-series signals. Unlike traditional neural networks, CNNs use convolutional layers to capture more complex structures, such as faults or anomalies in industrial systems. Pooling layers are also applied to reduce dimensionality and focus on important features and fully connected layers to perform classification or regression tasks.

II. Methods and Materials

Our proposed experimental framework for the automatic classification of faults in dynamic systems involves several key steps: data collection, preprocessing, model training, fine-tuning, hyper-parameter optimization, and model evaluation.In this work, we focus on the Hybrid Bond Graph as unified graphical method of modelling and diagnosis of hybrid systems with uncertain parameters. The diagnosis model was developed using the bond graph methodology and MATLAB software were used to obtain the dynamic behavior of the thermo-fluid system.Fig. 1 shows the simulation model, the diagnostic model and the CNN FDI, respectively.

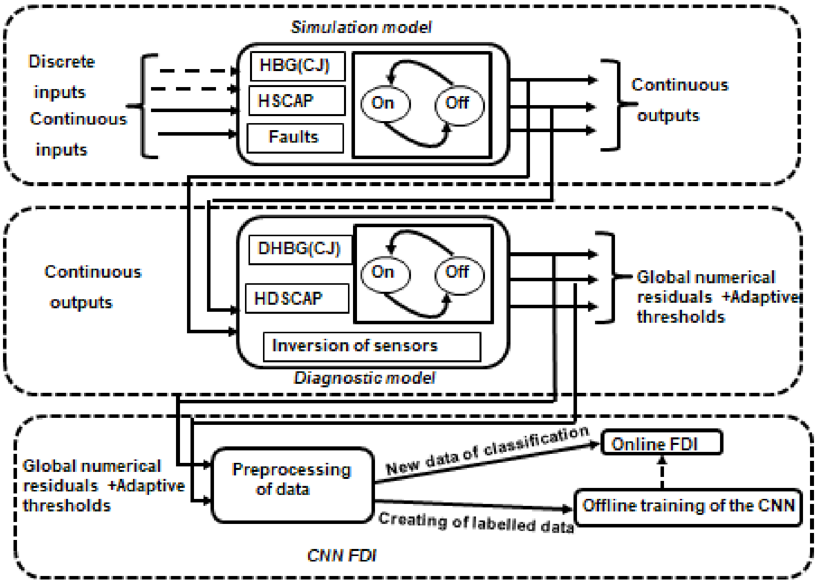

Fig. 1.Schematic diagram illustrating modeling and diagnosis with HBG approach.

2 Diagnosisof the thermo-fluid system

2.1Description of the thermo-fluid system

A thermo-fluid two-tank system [5] is in thermal-fluid sciences to study the dynamics of fluid flow, heat transfer, and system control, Fig. 2. It consists of:

- Two interconnected tanks(Tank$_i$, i=1,2) which can hold a working fluid.
- Pump Q$_p$and valves (V$_1$, V$_2$) to control fluid flow between the tanks.
- Heaters in one tank to provide thermal energy.
- Four sensors (T$_1$, T$_2$, L$_1$, L$_2$) to monitor temperature and fluid level.
- Two outlets (R$_{L1}$, R$_{L2}$) drainlliquid,are considered linear.

Here, for the realization of switched mode operation (i.e. mode change), we impose another condition that the valve V$_1$ (or V$_2$) is to be controlled (changing u$_1$ or u$_2$) such that the level L$_1$(t) (or L$_2$(t)) increases above L$_{D1}$ (or L$_{D2}$).

The outputs from the PI controller, u$_p$, and the pump flow (Q$_p$), given in Eq. (1) and (2), respectively, are measured.

$$u_p = K_p(S_{Pt} - \rho g L_1(t)) - K_I \int (S_{Pt} - \rho g L_1(t) dt = \Phi_{PI} L_1(t) \qquad (1)$$

$$Q_p = \Phi_p(u_p) = \begin{cases} u_p & \text{if } 0 \le \text{u}_p \le f_{\max} \\ 0 & \text{if } \text{u}_p \le 0 \\ f_{\max} & \text{if } \text{u}_p \succ f_{\max} \end{cases} \qquad (2)$$

where, K$_p$ and K$_I$are, respectively, the proportional and integral gains, and S$_{pt}$is predefined set point for the PI controller. The pump function is represented by Φ_p and the PI controller function is defined by Φ_{PI} .

The outflowQ$_t$ from the heater is also measured. The On-Off controller acts upon the heater to maintain the temperature in Tank$_1$ within some prescribed limit in accordanceto its control law given by:

$$u_0 = \Phi_0(T_1) = \begin{cases} 0 \text{ if } T_1 > T_{\max} \\ 1 \text{if } T_2 < T_{\min} \end{cases} \qquad (3)$$

where, u$_0$ represents the measured output from the On-Off controller and Φ_0 the On-Off controller function. We have considered a linear function for the heater output (Q$_t$), given by $Q_t = \Phi_t(u_0) = \kappa.u_0$, where, κ is the constant of proportionality for the heater. One condition is imposed on the heater function: The heater will remain off when $L_1(t)$ does not exceed a minimum level L_m whatever be the output signal from the On-Off controller, as shown in Eq. (4)

$$Q_t = a_1.\Phi_t(u_0), \text{where, } a_1 = \begin{cases} 0 \text{ if } L_1(t) \le L_m \\ 1 \text{ if } L_1(t) > L_m \end{cases} \quad (4)$$

The heater, as input source, gives a train of picks due to On-Off controller action which has been smoothened out passing the input controller signal through a low pass filter having phase lag of 30° and break frequency of 1 rad/s before going to the heater. The transfer function of the lag compensator thus designed is (0.3333s+0.577)/(s+0.577).

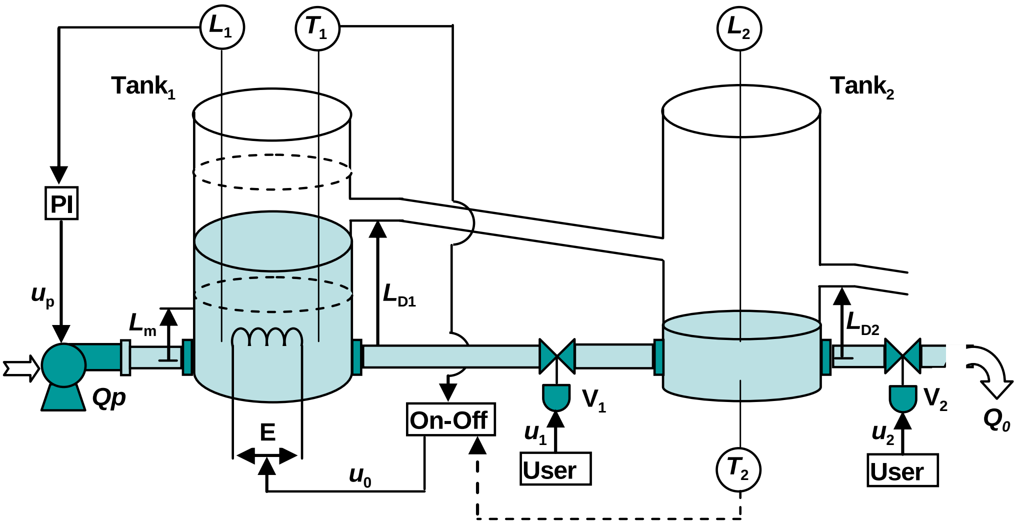

Fig. 2. Process and instrument diagram (P&ID) of the hybrid thermo-fluid Process

2.2 HBG and state space model of thermo-fluid system

Fig. 3 shows a word bond graph where the vertices represent subsystems or technological components denoted by a word and the inputs and outputs are power variables.

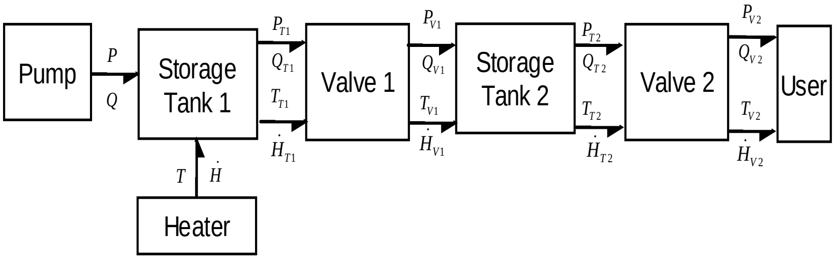

Fig. 3. Word bond graph of the thermo-fluid system

Hybrid systems consist of continuous dynamics and discrete behavior represented by modes. At each mode, the system is governed by continuous dynamics modelled by different continuous models. If the number of switches increases, a combinatorial explosion will take place. In order to overcome this problem, a fixed causality HBG is achieved even if the physical configuration changes [6,7, 8]. Formally, HBG can be defined as a triple: HBG = {BG, M, a}, where BG is the Bond Graph model, M = {M1 M2, ..., Mk} is a set of finite state of automata, and a is the mapping between each M, and a junction in the bond graph. Each M, is a finite state automaton of the type described above, with an output function that maps each state of M, to either on or off. The HBG model of thermo-fluid system is given in Fig.4.

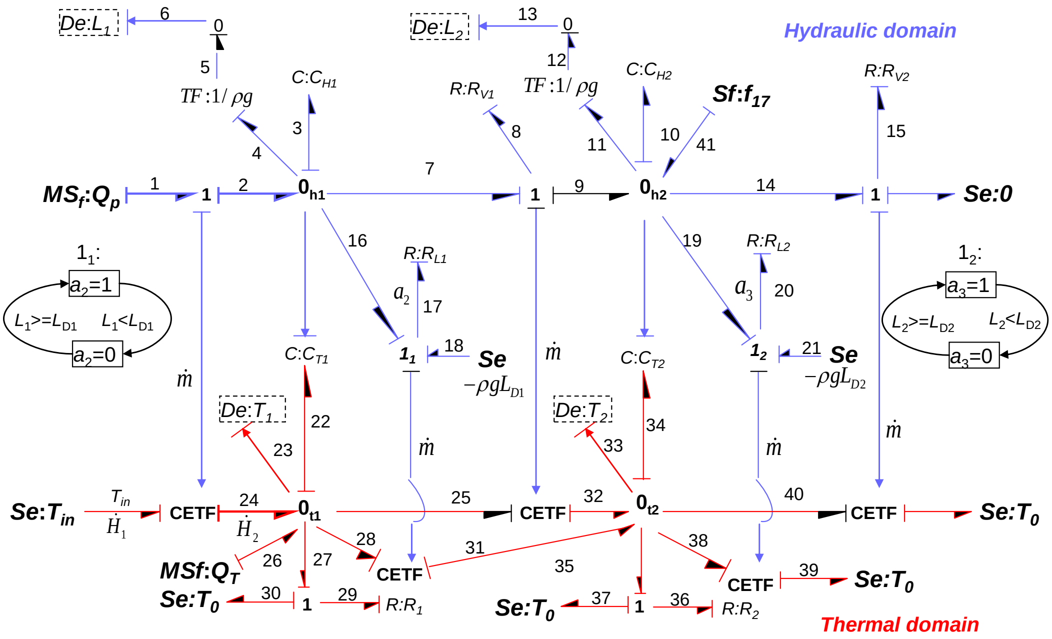

Fig. 4. Hybrid Bond Graph (HBG) model of the thermo-fluid system

The two sources into tank 1 are indicated by MSf and Se, respectively, the tank capacities are shown as C_{H1}, C_{H2}, C_{T1} and C_{T2}, and the pipes are modeled by resistances R_{V1}, R_{V2}, R_1 and R_2. The hydraulic and thermal capacities of the fluid in two tanks are given by $C_{Hi}=A_i/g$ and $C_{Ti}=m_ic_p$, for i=1,2, where m_i represents the stored mass of fluid in each tank. The states associated with C-elements in the hydraulic and thermal domains are mass (m) and enthalpy (H), respectively. BG elements R_1 and R_2 are used to model heat transfer to the environment. Note that the mass flow (f_{17}) coming out from Tank$_1$ through the bypass line (switched on mode) will enter the Tank$_2$ in same quantity, which is modeled by Sf: f_{17} (refer bond No. 41). Along with the mass flow some enthalpy will also get transferred to the downstream side as modeled by CETF element appended to bond 28 and 31. CETF represents the Coupling Element for Thermo-Fluids [9]. Two possible causal forms of CETF and the corresponding equations are given in Table 1, where c_p is the specific heat capacity of the fluid.

Table 1 Causal forms of the CETF element

Causal form of the CETF	Equation
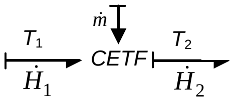	$\dot{H}_1 = \dot{m}c_pT_1$ $\dot{H}_2 = \dot{m}c_pT_1$
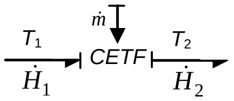	$T_1 = \frac{\dot{H}_1}{\dot{m}c_p}$ $\dot{H}_2 = \dot{H}_1$

The top part of HBG model (Fig. 4) concerns hydraulic domain and the bottom part concerns thermal domain. The control signals for turning these junctions on and off are generated by the finite state automata in Fig. 4. For autonomous transition in the system, also modeled by controlled junctions, the transition conditions computed from system variables (e.g., see the transition condition for junctions 1_1 and 1_2). A mode in the system is defined by the state of the two controlled junctions in the HBG model. Therefore, theoretically, the system can be in 2^2 different modes.

The state equation form can be systematically deduced from HBG in non-linear form:

$$\begin{cases} \dot{x} = F(x,u) \\ y = G(x,u) \end{cases} \tag{5}$$

where x is the state vector and u is the input vector. The state vector x of thermo-fluid system is composed of the variables m_1(mass of water in Tank 1), m_2 (mass of water in Tank 2), H_1 (enthalpy in Tank 1) and H_2 (enthalpy in Tank 2).

The structural equations are the constitutive equations of 0 and 1 junctions

$$\begin{cases} \mathrm{o}_{h1} \text{ junction: } f_3 = f_2 - f_7 - a_2 f_{16} \\ \mathrm{o}_{h2} \text{ junction: } f_{10} = f_9 + a_2 f_{41} - f_{14} - a_3 f_{19} \\ \mathrm{o}_{t1} \text{ junction: } f_{22} = f_{24} + f_{26} - f_{25} - a_2 f_{28} - f_{27} \\ \mathrm{o}_{t2} \text{ junction: } f_{34} = a_2 f_{31} + f_{32} - f_{40} - a_3 f_{38} - f_{35} \end{cases} \tag{6}$$

The following equations are the constitutive behavioral of bond graph C and Relements:

$$\begin{cases} f_3 = \dot{m}_1, f_{10} = \dot{m}_2, f_{22} = \dot{H}_1, f_{34} = \dot{H}_2, f_2 = Q_p, f_{26} = Q_T, f_{24} = Q_p c_p T_0 \\ f_7 = f_9 = Cd_1.u_1\sqrt{\left|\frac{m_1}{C_{H1}} - \frac{m_2}{C_{H2}}\right|} \\ f_{16} = f_{41} = \frac{1}{R_{L1}}(\frac{m_1}{C_{H1}} - \varphi g L_{D1}) \\ f_{14} = Cd_2.u_2\sqrt{\left|\frac{m_2}{C_{H2}}\right|} \\ f_{19} = \frac{1}{R_{L2}}(\frac{m_2}{C_{H2}} - \varphi g L_{D2}) \\ f_{25} = f_{32} = Cd_1.u_1\sqrt{\left|\frac{m_1}{C_{H1}} - \frac{m_2}{C_{H2}}\right|}\frac{H_1}{m_1} \\ f_{27} = \frac{1}{R_1}(\frac{H_1}{C_{T1}} - T_0) \\ f_{28} = f_{31} = \frac{1}{R_{L1}}(\frac{m_1}{C_{H1}} - \varphi g L_{D1})\frac{H_1}{m_1} \\ f_{40} = Cd_2.u_2\sqrt{\left|\frac{m_2}{C_{H2}}\right|}\frac{H_2}{m_2} \\ f_{38} = \frac{1}{R_{L2}}(\frac{m_2}{C_{H2}} - \varphi g L_{D2})\frac{H_2}{m_2} \\ f_{35} = \frac{1}{R_2}(\frac{H_2}{C_{T2}} - T_0) \end{cases} \tag{7}$$

Combining equations (6) and (7), we obtain the state space equations:

$$
\left\{
\begin{aligned}
&\dot{m}_1 = -Cd_1.u_1\sqrt{\left|\frac{m_1}{C_{H1}}-\frac{m_2}{C_{H2}}\right|} - a_2\frac{1}{R_{L1}}\left(\frac{m_1}{C_{H1}}-\varphi g L_{D1}\right) + Q_p\\
&\dot{m}_2 = Cd_1.u_1\sqrt{\left|\frac{m_1}{C_{H1}}-\frac{m_2}{C_{H2}}\right|} + a_2\frac{1}{R_{L1}}\left(\frac{m_1}{C_{H1}}-\varphi g L_{D1}\right) - Cd_2.u_2\sqrt{\left|\frac{m_2}{C_{H2}}\right|} - a_3\frac{1}{R_{L2}}\left(\frac{m_2}{C_{H2}}-\varphi g L_{D2}\right)\\
&\dot{H}_1 = -Cd_1.u_1\sqrt{\left|\frac{m_1}{C_{H1}}-\frac{m_2}{C_{H2}}\right|}\frac{H_1}{m_1} - a_2\frac{1}{R_{L1}}\left(\frac{m_1}{C_{H1}}-\varphi g L_{D1}\right)\frac{H_1}{m_1} - \frac{1}{R_1}\left(\frac{H_1}{C_{T1}}-T_0\right) + Q_p c_p T_0 + Q_T\\
&\dot{H}_2 = a_2\frac{1}{R_{L1}}\left(\frac{m_1}{C_{H1}}-\varphi g L_{D1}\right)\frac{H_1}{m_1} + Cd_1.u_1\sqrt{\left|\frac{m_1}{C_{H1}}-\frac{m_2}{C_{H2}}\right|}\frac{H_1}{m_1} - Cd_2.u_2\sqrt{\left|\frac{m_2}{C_{H2}}\right|}\frac{H_2}{m_2}\\
&-a_3\frac{1}{R_{L2}}\left(\frac{m_2}{C_{H2}}-\varphi g L_{D2}\right)\frac{H_2}{m_2} - \frac{1}{R_2}\left(\frac{H_2}{C_{T2}}-T_0\right)
\end{aligned}
\right. \tag{8}
$$

$$
y = \begin{bmatrix} L_1 \\ L_2 \\ T_1 \\ T_2 \end{bmatrix} = \begin{bmatrix} \frac{1}{\varphi A_1} & 0 & 0 & 0 \\ 0 & \frac{1}{\varphi A_2} & 0 & 0 \\ 0 & 0 & \frac{1}{m_1 c_p} & 0 \\ 0 & 0 & 0 & \frac{1}{m_2 c_p} \end{bmatrix} \begin{bmatrix} m_1 \\ m_2 \\ H_1 \\ H_2 \end{bmatrix}
$$

This model is simulated in Matlab software. More details of sequential ordering to obtain state equations are given in [10].

2.3 GARR limits with non-invertible constraints

The DHBG model of thermo-fluid system is given in Fig. 5. The existing methods for derivation of the GARR from a hybrid bond graph model are not well structured and they cannot be applied, when unknown variables cannot be eliminated because of the presence of algebraic loops and non-linear non-invertible constraints [11].

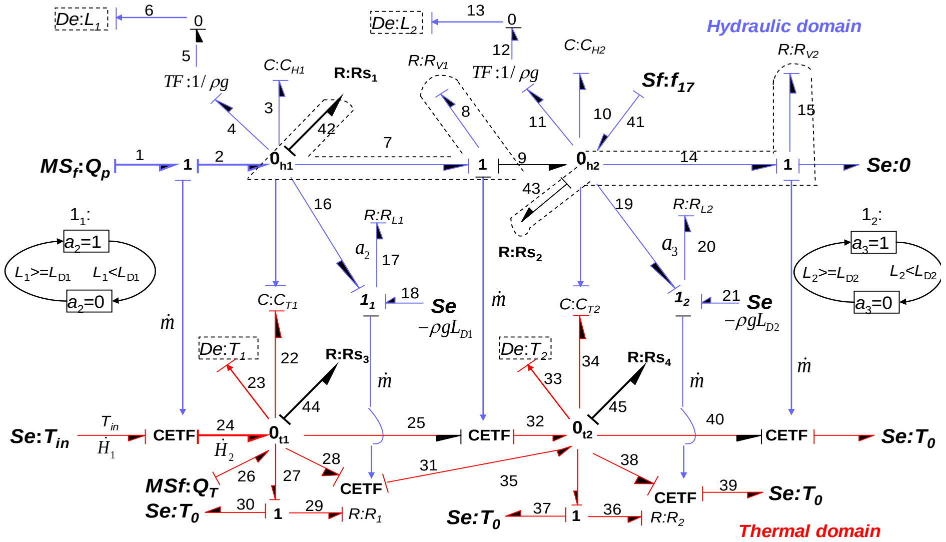

Fig. 5. Diagnosis Hybrid bond graph model of the thermo-fluid process

To introduce this problem, take as example from the model in (Fig. 5), an algebraic loop between R_{s1} and R_{v1} (marked by dotted lines in Fig. 5) and the constitutive relation of the junction o_{h2} is given by the following equation:

$$f_8 - f_{10} - f_{43} - f_{19} + f_{41} = 0 \ (9)$$

The Eq. (9) can be a GARR if all variables f_8, f_{10}, f_{43}, f_{19}, and f_{41} are known. If we admit that the causality affected to R_{v1} is fixed and corresponded to (Fig. 5), its constitutive relation, between the flow variable f_8 and the effort variable e_8, can be determined by the following non-linear relation:

$f_8 = \Phi_{V1}(e_8)$ (10)

where Φ_{V1} non-invertible relation.

The algebraic loop between R_{v1} and R_{s1} is expressed analytically by the following relation:

$$\begin{aligned} f_8 &= \Phi_{V1}(e_8) \\ &= \Phi_{V1}(e_7 - e_9) = \Phi_{V1}(e_{42} - P_2) = \Phi_{V1}(\Phi_{Rs1} f_{42} - P_2) \\ &= \Phi_{V1}(\Phi_{Rs1}(f_2 - f_3 - a_2 f_{17} - f_8) - P_2) \\ &= \Phi_{V1}(\Phi_{Rs1}(Q_p - C_{H1}\frac{dP_1}{dt} - a_2(\frac{P_1 - \varphi g L_{D1}}{R_{L1}}) - f_8) - P_2) \\ &= \Psi_1(Q_p, P_1, f_8, L_{D1}, P_2) \end{aligned} \qquad (11)$$

Eq. 11 expresses a loop algebraic. So the conventional method of generating GARR is inconvenient. Recently, the causality inversion of detectors (or putting them as sources) has been proposed as a unified approach to generate residuals. Residuals are generated using the conversation laws at each junction (1 and 0) and then their structural independence are checked with existing residuals. On the contrary, the substitutions presented in this paper are derived from a systematic treatment, which are not aimed at obtaining a closed from symbolic GARR. Only structurally independent residuals are generated by using the method presented in this work

2.4Generation of residuals

First of all, we define a sensor element, Ds, to measure a signal without qualitatively assigning the nature of signal, i.e. effort or flow, to the device. The device measuring the output from a controller is represented as a signal sensor, Ds. When the causality of the signal sensor, Ds, is inverted, we represent it as an element for a signal source, called Ss. This element, Ss, has already been proposed in [12], as a source sensor for use in the more general application for system inversion in the design of the control laws. When the preferred differential causality is assigned to the bond graph model using inversion of the sensor causalities, if necessary, the following five compositions are possible. The causalities of the output ports of sensors, which may be connected to controllers, are not inverted [13, 14].

Consider the 0-junction connected to effort sensor De with inverted causality, the conservation relation for the 0-junction leads to

$$f_{De} = \sum_{i\_in=1}^{n} f_{i\_in} - \sum_{i\_out=1}^{n} f_{i\_out} \qquad (12)$$

where f_{i_in} and f_{i_out} are inflows and outflows of 0-junction, respectively. f_{De} is the flow variable corresponding to the effort sensor De. Since $f_{De} = 0$, the Eq. (12) becomes:

$$\sum_{i\_in=1}^{n} f_{i\_in} - \sum_{i\_out=1}^{n} f_{i\_out} = 0 \qquad (13)$$

which, once f_{i_in} and f_{i_out} calculated, leads to a GARR. However, in the case of non-invertible causal constraints, elimination of the unknown variables is not possible. We must solve numerically the Eq. (13) to obtain the residual.

From the DHBG model of the thermo-fluid system in Fig. 5, the numerical values for the residuals can be obtained. However, for FDI, the fault signature matrix, S, should be available. Analysis of the causal paths to each residual is used to generate these signatures. As an example, the virtual sensor for residual r6 is represented in the bond number 46 in Fig. 6.

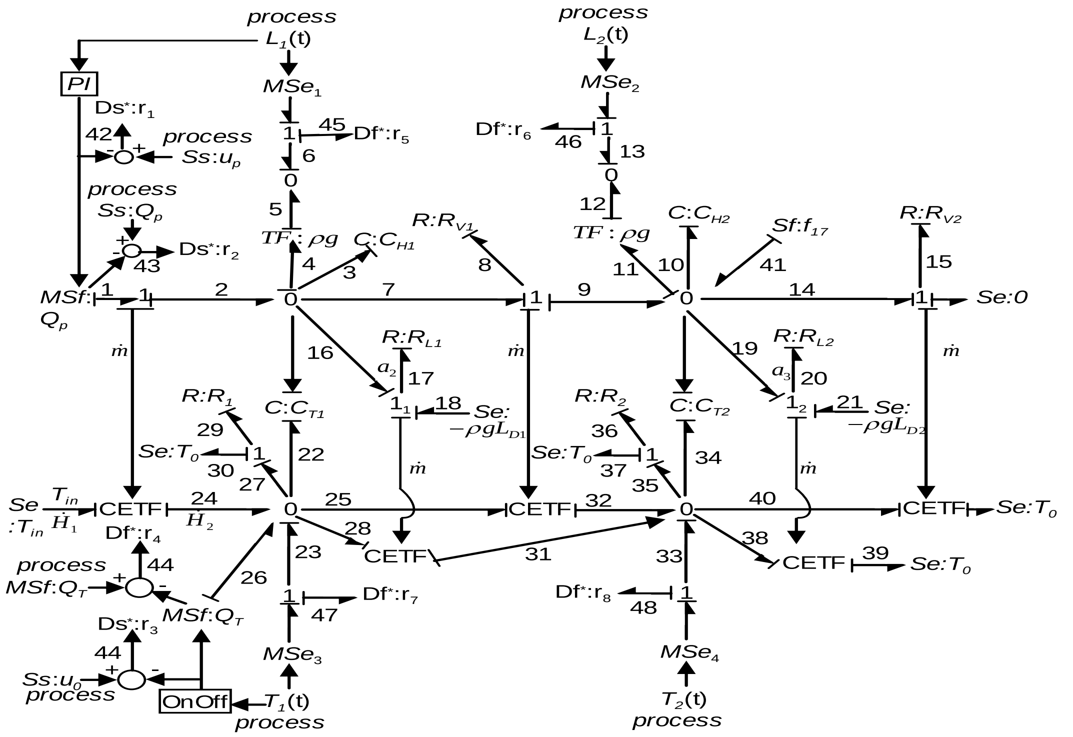

Fig. 6. DHBG model and numerical residuals of the thermo-fluid system.

The following are the causal paths to residual r6.

1. $Mse_2 \rightarrow e_{13} \rightarrow e_{12} \rightarrow e_{11} \rightarrow e_{14} \rightarrow e_{15} \rightarrow R_{v2} \rightarrow f_{15} \rightarrow f_{14} \rightarrow f_{11} \rightarrow f_{12} \rightarrow f_{13} \rightarrow f_{46}$.
2. $Mse_2 \rightarrow e_{13} \rightarrow e_{12} \rightarrow e_{11} \rightarrow e_9 \rightarrow e_8 \rightarrow R_{v1} \rightarrow f_8 \rightarrow f_9 \rightarrow f_{11} \rightarrow f_{12} \rightarrow f_{13} \rightarrow f_{46}$

From these causal paths, the components involved in the residual r6 are obtained as K_6= [$V_1(C_{d1})$, $V_2(C_{d2})$]. The fault signature matrix, S, for the device (components) of the thermo-fluid system, in Fig. 2, is given in Table 2. The fault detectability and fault isolability of each parameter is gained from the {D_b, I_b} values.

Table 2: FSM for Thermo-Fluid Process

	r_1	r_2	r_3	r_4	r_5	r_6	r_7	r_8	D_b	I_b
Pump	1	1	0	0	1	0	1	0	1	1
Heater	0	0	1	a_1	0	0	0	0	1	1
$V_1(C_{d1})$	0	0	0	0	1	1	1	1	1	$\bar{a}_2$
$V_2(C_{d2})$	0	0	0	0	a_2	1	a_2	1	1	$\bar{a}_2 \times \bar{a}_3$

.

2.5 Residual thresholds

Adaptive thresholds are designed to achieve robustness in fault diagnosis. The robustness is particularly achieved with respect to parameter uncertainties so as to avoid misdetections and false alarms.

We have designed the adaptive thresholds using the Linear Fractional Transformation (LFT) model (reference) whereby the parameter uncertainties are separated from the nominal model [15, 16]. Figure7 represents the DHBG of LFT form for the thermo-fluid system:

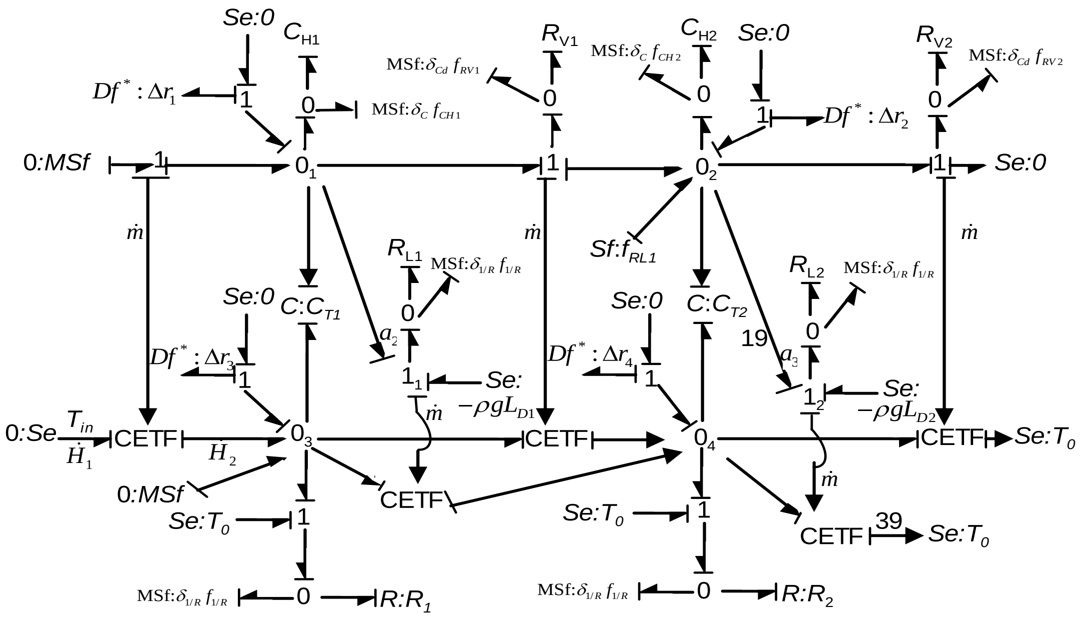

Fig. 7. DHBG of the thermo-fluid system in LFT form

As an example, when the actual value of a C-element is not perfectly known, it can be written as $C_n \pm \Delta C$, where C_n is the nominal value and $\pm\Delta C$ is the uncertainty in the parameter. For the R-element, it can be written as $R_n \pm \Delta R$, where R_n is the nominal value and $\pm\Delta R$ is the uncertainty in theparameter. Finally, For the L-element, it can be written as $L_n \pm \Delta L$, where L_n is the nominal value and $\pm\Delta L$ is the uncertainty in the parameter.

III. Residuals simulation

Figures 8 and 9 represent the block diagram model drawn in Simulink representing the DHBG of the thermo-fluid system and the block diagram of the incremental DHBG model, respectively.

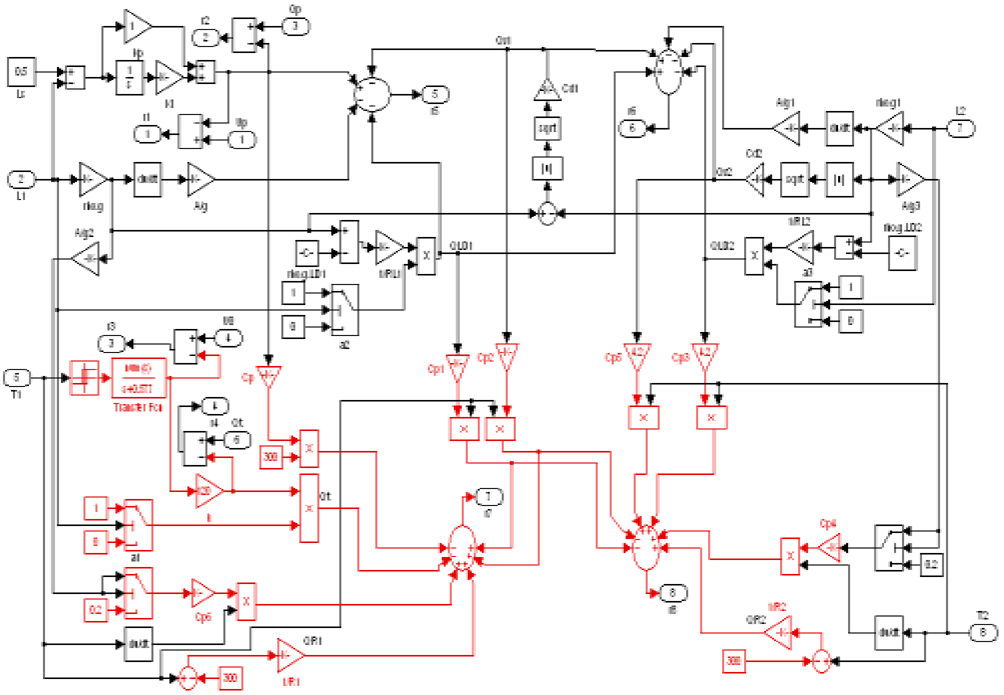

Fig. 8. Matlab-simulink block Diagram model of the DHBG of thermo-fluid system.

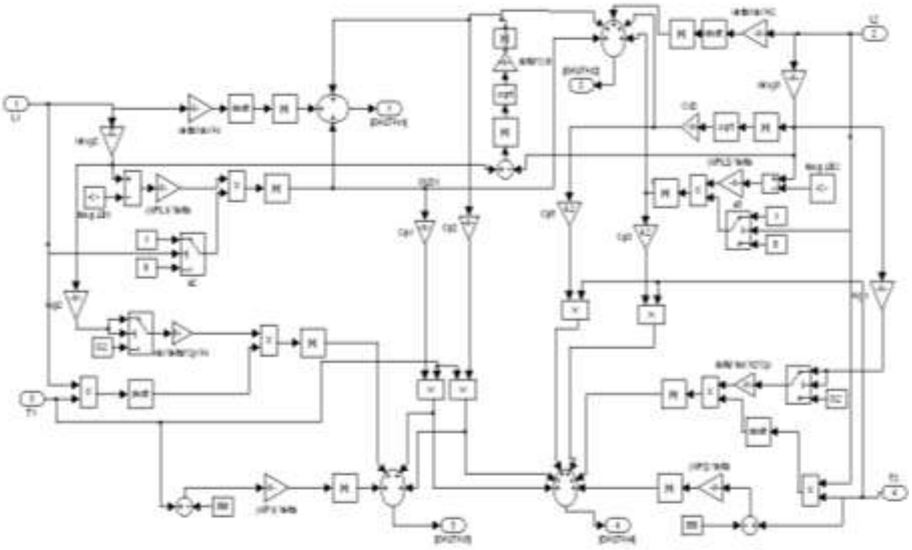

Fig. 9. Matlab-simulink block Diagram model of the incremental DHBG of thermo-fluid system.

To simulate reality, noise is added to sensor outputs from the behavioral model before being input to the DHBG. The noise magnitude is chosen at 2% of each sensor's output. The block diagram representation of the sensor output with noise is given in Fig.10.

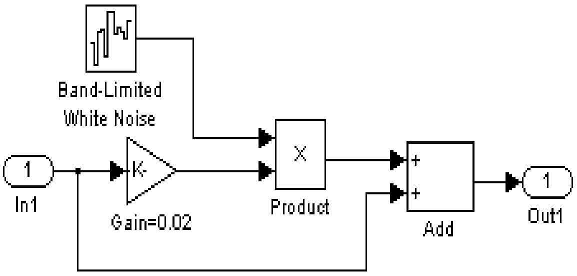

Fig. 10. Block diagram of the sensor data model

In this work, MATLAB R2021b is used to simulate the model of the thermo-fluid systemwith a fixed step size of 0.001s for duration of 600s. The all state variables are initialized to zero. The nominal parameter values considered for the model are given in table 3.

Table 3: Nominal model parameters of the thermo-fluid process

Symbol	Description	Value
Kp	Proportional gain of controller	1 m.s
K_i	Integral gain of controller	5×10^{-2} m
L_s	Set point of the PI controller	0.5 m
f_{max}	Maximum outflow from pump	0.8kg.s^{-1}
A_i	Cross-sectional area of Tank$_i$ (i=1,2)	1.54×10^{-2} m^2
C_{d1}	Discharge co-efficient of valve V_1	1.593×10^{-2} (kg.m)$^{0.5}$
C_{d2}	Discharge co-efficient of valve V_2	1.593×10^{-2} (kg.m)$^{0.5}$
R_{L1}	Drainage resistance from Tank$_1$	1.25×10^3 m^{-1}s^{-1}
R_{L2}	Drainage resistance from Tank$_2$	1×10^3 m^{-1}s^{-1}
P_{atm}	Atmospheric pressure (gage)	0 N.m^{-2}
c_p	Specific heat capacity of water	4.2 kJ/kg.K
T_0	Ambient temperature	300 K
L_m	Minimum level required in Tank$_1$ for starting of heater actuation	0.48 m
L_{D1}	Height of the bypass drain of Tank$_1$ from common datum	0.51 m
L_{D2}	Height of the secondary drain of Tank$_2$ from common datum	0.27 m
T_{max}	Maximum temperature set point of On-Off controller	330 K
T_{min}	Minimum temperature set point of On-Off controller	320 K
K	Constant for the heater function	120 kJ/s
R_1	Thermal resistance to conductive heat loss from Tank$_1$	10 kJ^{-1}K.s
R_2	Thermal resistance to conductive heat loss from Tank$_2$	10 kJ^{-1}K.s

The residual signals can be generated with an adaptive threshold in the shape of envelope, as depicted in Fig.11. For the case of fault detection, if the value of residual crosses its threshold, then an alarm is generated. The uncertainly in each parameter value is considered to be ± 2%.

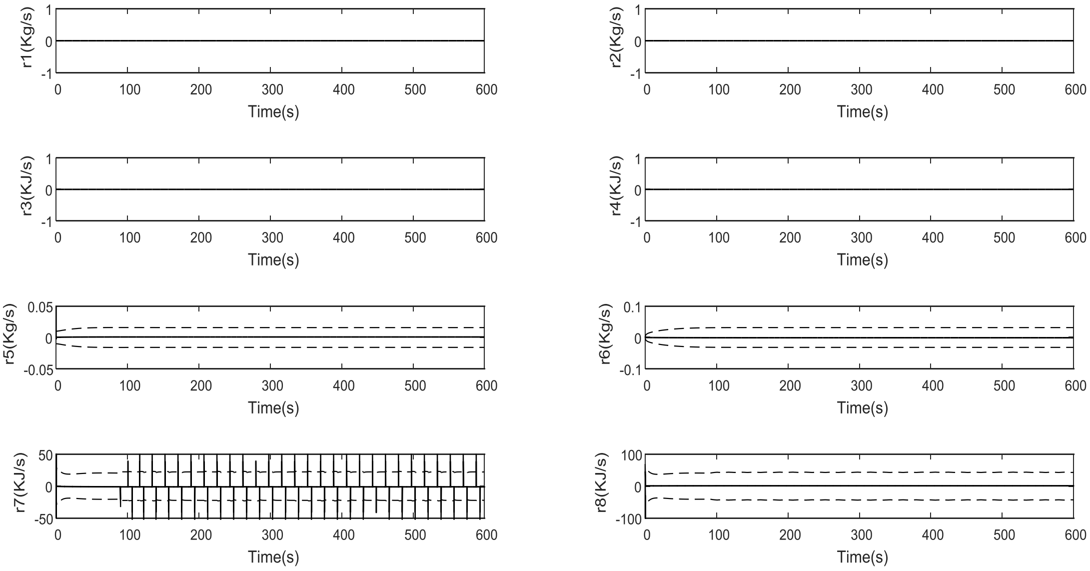

Fig. 11. The LFT GARRs with its adaptive thresholds

IV. Hyper parameter Optimization and Model Configuration

In Deep Learning (DL), model performance is highly dependent on the appropriate selection and tuning of hyper-parameters. These hyper-parameters must be carefully optimized through iterative experimentation to minimize prediction error and enhance classification accuracy, robustness, and generalization capability. Some hyper-parameters are common across most DL architectures, while others are model-specific. Since no analytical rule exists to determine optimal hyper-parameter values, systematic search strategies, empirical evaluation, and domain expertise are typically employed.Common hyper-parameters include the learning rate, number of epochs, batch size, optimizer selection, early stopping criteria, and the choice of loss function. These parameters directly affect the convergence behavior of the training process, which is governed by gradient-based optimization. Model parameters θ are updated iteratively using gradient descent according to

$$\theta_{t+1}=\theta_t-\eta\nabla\theta L(\theta_t) \qquad (14)$$

where η denotes the learning rate and L represents the loss function.

In addition to these general hyper-parameters, model-specific parameters must also be tuned based on the application domain, dataset characteristics, and computational constraints. These include activation functions, the number and structure of dense layers, convolutional parameters such as kernel size and number of filters, dropout rates, stride, and padding [17, 18, 19].

4.1 Optimization Strategy

To optimize the common hyper-parameters, multiple configurations were evaluated by systematically varying parameter values across increasing and decreasing ranges. Initially, a high number of epochs (100) was selected as a baseline to ensure sufficient convergence. This value was subsequently refined for each architecture using early stopping to prevent overfitting.Learning rates ranging from 10^{-8} to 10^{-1}, batch sizes between 3 and 50, and several widely used optimizers—including Stochastic Gradient Descent (SGD), Adam, RMSProp, and Adadelta—were evaluated. The Adam optimizer was of particular interest due to its adaptive learning rate mechanism, which combines first- and second-order moment estimates:

$$m_t=\beta_1 m_{t-1}+(1-\beta_1)g_t$$

$$v_t=\beta_2 v_{t-1}+(1-\beta_2)g_t^2 \qquad (15)$$

$$\theta_{t+1}=\theta_t-\eta\frac{\hat{m}_t}{\sqrt{\hat{v}_t}+\varepsilon}$$

where $g_t = \nabla_\theta L(\theta_t)$.

4.2 Loss Functions

For multi-class classification, the categorical Cross-Entropy loss was primarily employed:

$$L_{CE} = -\sum_{i=1}^{C} y_i \log(\hat{y}_i) \qquad (16)$$

where C is the number of classes, yi is the ground-truth label, and yi is the predicted probability.To address potential class imbalance and improve learning on difficult samples, the Focal Cross-Entropy loss was also investigated:

$$L_{Focal} = -\sum_{i=1}^{C} (1-\hat{y}_i)^{\gamma} y_i \log(\hat{y}_i) \qquad (17)$$

where γ is the focusing parameter that increases the contribution of misclassified samples.

4.3Cross-Validation and Optimal Hyper-parameters

To ensure robust performance and mitigate overfitting, k-fold cross-validation was applied with k ranging from 5 to 15, providing a balance between computational cost and statistical reliability.Following extensive experimentation, the optimal configuration was obtained with a learning rate of 0.001, the Adam optimizer, 10 training epochs, and a batch size of 10.

4.4CNN Architecture and Model-Specific Parameters

The optimized Convolutional Neural Network (CNN) architecture is illustrated in Figure 12.A. The model comprises four convolutional layers, where each convolution operation is defined as:

$$X^{(l)} = f(W^{(l)} * X^{(l-1)} + b^{(l)}) \qquad (18)$$

with* denoting convolution, f the activation function (ReLU), and $W^{(l)}$ and $b^{(l)}$ the trainable weights and biases. Two max-pooling layers are employed to reduce spatial dimensionality, and dropout regularization is applied to mitigate overfitting. Dropout is defined as:

$$\tilde{h} = h \odot m, m \sim Bernoulli(p) \qquad (19)$$

where p is the probability of retaining an active neuron.

The convolutional layers are followed by two fully connected layers with 256 and 5 neurons, respectively, where the final layer corresponds to the number of fault classes.

4.5Performance Evaluation

Figure 12.B presents the confusion matrix, demonstrating perfect classification across all classes: healthy, valve1, valve2, pump, heat, and multi-fault conditions. All non-zero values lie on the main diagonal, indicating zero misclassification. This confirms that the extracted fault signatures are well separated and that the proposed CNN exhibits excellent discrimination capability, even for multi-fault scenarios.Figure 12.C shows the training and validation accuracy and loss curves. The model converges rapidly, achieving 100% accuracy on both datasets by the third epoch, with no observable generalization gap. The loss decreases sharply during the initial epochs and stabilizes near zero thereafter. Although such early convergence should be interpreted with caution, these results strongly suggest that the Bond Graph residuals provide highly discriminative features for fault diagnosis, including complex multi-fault cases.

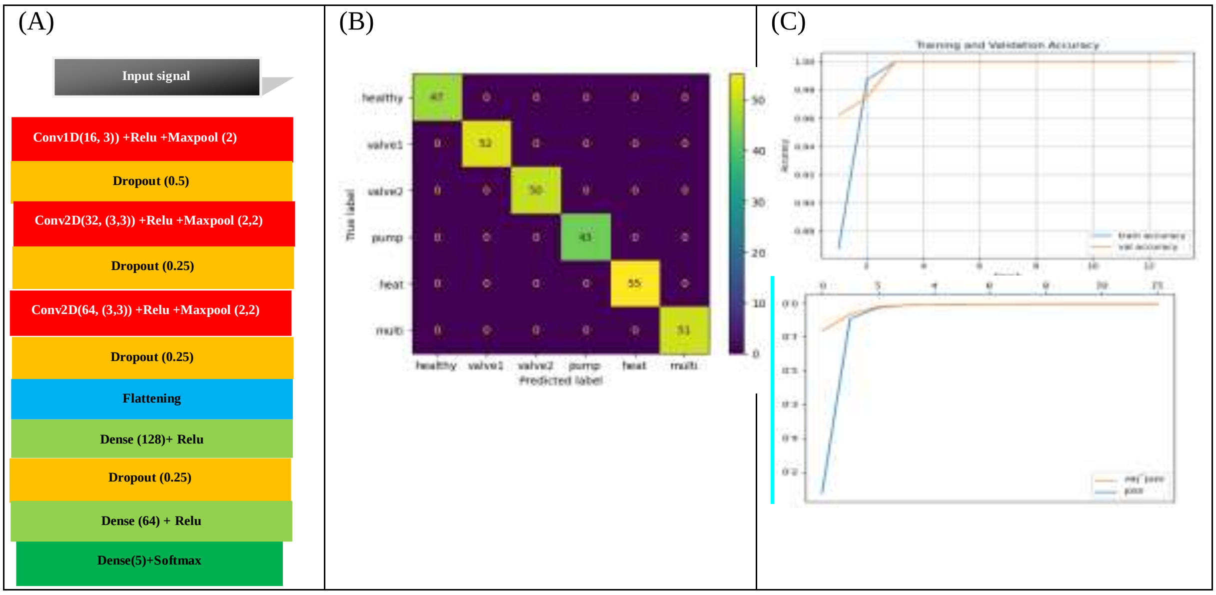

Fig.12. Schematic diagram illustrating the main steps for defaults classification in complex dynamic system practice: (A) our fine-tuned CNN; (B) Confusion matrix of the proposed method; and (C) accuracy-loss curves of the fine-tuned model.

In summary, the model learns the underlying fault patterns very efficiently, as this is evident by the rapid decrease in the loss function. Perfect convergence is achieved after only a few training epochs, indicating that the class representations are well separated in the feature space. No signs of overfitting are observed, since the training and validation losses remain closely aligned throughout the learning process, demonstrating strong generalization performance on the validation set.

Nevertheless, several limitations of this study should be acknowledged:

1. Although the proposed Bond Graph modeling combined with Convolutional Neural Networks (CNNs) achieved promising results in fault classification, the study is based on a relatively small dataset comprising only 500 real samples. This limited sample size may restrict the model's ability to generalize to unseen and more diverse fault patterns.
2. The small dataset may have resulted in slightly optimistic performance estimates, which could differ when the models are evaluated on larger, independent datasets.
3. Model validation was performed exclusively using data collected from a single industrial source. To improve the robustness, generalizability, and practical applicability of the proposed approach, external validation using data from multiple sites is necessary. Such validation should incorporate greater variability in operating conditions, fault types, and system configurations, thereby enabling further refinement of the models.
4. Although numerous fault detection and classification methods have been proposed over recent decades, a systematic comparison with classical baseline techniques and alternative machine learning approaches is still required to objectively assess the relative merits and advances of the proposed method.
5. This study relied solely on data from five fault modalities (e.g., valve1, valve2, pump, heat, and multi-fault). Incorporating additional fault modes and multimodal data sources could enhance the robustness and generalizability of the proposed framework by improving fault detection and classification capabilities.

Addressing these limitations in future work is expected to further improve both the performance and interpretability of the method.

V. Conclusion

The method presented in this paper enhances the availability of the information for the decision support system by generating all the structurally independent residuals in numerical form. This is important in situations where symbolic form of the residuals cannot be obtained, due to the presence of various forms of loops in the equations of the mathematical model. The algorithm to generate the numerical residuals is directly obtained from the bond graph model of the system using the set of substitutions. This leads to a graph structure, called a diagnosis hybrid bond graph (DHBG) model, where sensor data from the system or the process are the inputs and the residuals are the outputs. Analysis of the causal paths to the residuals on the diagnosis hybrid bond graph model is then used to generate the theoretical fault signature matrix. Simulation studies have been performed on a thermos-fluid system to show, how numerical residuals improve the overall performance of the decision procedure. Finally, it is important to note that the method presented in this paper can be applied to models containing different forms of non-resolvable loops and also to those, which do not contain any loops. System diagnostic methods typically consider only single faults. To generate fault indicators, a certain number of sensors must be installed. This solution is bulky for the system and expensive. CNNs make it possible to handle both multiple and single faults while using a reduced number of sensors.

References

[1]. D. De Scuter, “Optimal control of a class of linear hybrid systems with saturation”, SIAM Journal of Control Optimization, Vol. 39, No. 3, pp. 834-851, 2000.

[2]. R. Cacho, J. Felez, and C. Vera, Deriving simulation models from bond graphs with algebraic loops: the extension to multibond graph systems, Journal of the Franklin Institute Vol. 337, No. 5, pp. 579–600, 2000.

[3]. W. Borutzky, Supporting the generation of a state space model by adding tearing information to the bond graph, Simulation Practice and Theory Vol. 7, pp. 419–438, 1999.

[4]. W. Borutzky, and F.E. Cellier, Tearing algebraic loops in bond graphs, Transactions of the Society of Computer Simulation International, Vol. 13, No 2, pp. 102–115, 1996.

[5]. S. K. Gholshal, S. Samanta and A. K. Samantary: Robust fault detection and isolation of hybrid systems with uncertain parameters. Journal of Systems and Control Engineering (JSCE), pp. 1013-1028, July 2012.

[6]. C. B. Low, D. Wang, S. Arogeti and J. B. Zhang : Quantitative Hybrid Bond Graph-Based Fault Detection and Isolation, IEEE Trans. Autom. Sci. Eng. Vol.7, No, pp. 558-569, 2010.

[7]. D. Wang, M. Yu, C. B. Low, S. Arogeti. (ed.) (2013). Model-based Health Monitoring of hybrid systems. Chapter 2 : Hybrid systems and HBG models. Springer New York Heidelberg Dordrecht London.

[8]. W. Borutzky. Fault indicators and mode dependent state equations from a fixed causality diagnostic bond graph of linear models with ideal switches. Journal of Systems and Control Engineering (JSCE), pp. 1-14, November 2017.

[9]. B. OuldBouamama, K. Medjaher: Supervision of an industrial steam generator. Part I: Bond graph modelling. Control Engineering Practice, Vol. 14, No. 1, pp. 71-83, 2006.

[10]. A. Mukherjee, R. Karmakar, Modelling and Simulation of Enginnering Systems through Bonds graphs. Alpha Sciences International, pangbourne, UK, 2000.

[11]. K. Medjaher. Contribution de l’outil bond graph pour la conception de systèmes de supervision des processus industriels. Thèse de doctorat. Université des sciences et technologies, 2005.

[12]. P.J. Gawthrop: Physical interpretation of inverse dynamics using bicausal bond graphs, Journal of the Franklin Institute, pp. 743–769, 2000.

[13]. W. Borutzky,: Residual bond graph sinks for numerical evaluation of analytical redundancy relations in model based single fault detection and isolation. In Proc. 20th European conferenceon modelling and simulation (ECMS’06), pages 166-172, sanktAugustin, Germany, May 2006.

[14]. K. Medjaher, A. K. Samantary, B. O. Bouamama. Diagnostic bpnd graphs for direct residual evaluation. In International conference on Bond Graph Modeling and Simulation (ICBGM’05), pages 307-312. Simulation series, Vol.37, No.1, ISBN: 1:56555-287-3, 2005.

[15]. M. A. Djeziri, R. Merzouki, B. OuldBouamama, and G. Dauphin-Tanguy. Robust fault diagnosis using bond graph approach. IEEE/ASME Transactions on Mechatronics, To appear, 2007.

[16]. M. A. Djeziri, R. Merzouki, B. OuldBouamama, and G. Dauphin-Tanguy. Robust fault diagnosis using bond graph approach. IEEE/ASME Transactions on Mechatronics, To appear, 2007.

[17]. B. M. Dash, B. O. Bouamama, M. Boukerdja, K. M. Pekpe, “Bond Graph-CNN based hybrid fault diagnosis with minimum labeled data”, Engineering Applications of Artificial Intelligence 131, 2024

[18]. J.Faouzi,” Time Series Classification: A Review of Algorithms and Implementations”.In: Machine Learning (Emerging Trends and Applications), Proud Pen, 1-34, 2022.

[19]. R. Ayllón-Gavilán et al., “Convolutional- and Deep Learning-Based Techniques for Time Series Ordinal Classification,” IEEE Transactions on Cybernetics, Vol. 55, No. 2, February 2025.